

An Evidence Based Search For Gravitational Waves From Neutron Star Ring-downs

James Clark,^{*} Ik Siong Heng,[†] Matthew Pitkin,[‡] and Graham Woan[§]
Department of Physics and Astronomy, Kelvin Building, Glasgow G12 8QQ, UK

(Dated: March 28, 2007)

The excitation of quadrupolar quasi-normal modes in a neutron star leads to the emission of a short, distinctive, burst of gravitational radiation in the form of a decaying sinusoid or ‘ring-down’. We present a Bayesian analysis method which incorporates relevant prior information about the source and known instrumental artifacts to conduct a robust search for the gravitational wave emission associated with pulsar glitches and soft γ -ray repeater flares. Instrumental transients are modelled as sine-Gaussian and their evidence, or marginal likelihood, is compared with that of Gaussian white noise and ring-downs via the ‘odds-ratio’. Tests using simulated data with a noise spectral density similar to the LIGO interferometer around 1 kHz yield 50% detection efficiency and 1% false alarm probability for ring-down signals with signal-to-noise ratio $\rho = 5.5$. For a source at 15 kpc this requires an energy of $2.8 \times 10^{-5} M_{\odot} c^2$ to be emitted as gravitational waves.

I. INTRODUCTION

A possible mechanism for the emission of gravitational waves from neutron stars is the excitation of non-radial quasi-normal modes (QNMs) [1]. This excitation could be caused by the disruption associated with pulsar glitches [2] or from flaring activity in soft γ -ray repeaters [3].

The frequencies and damping times of the QNMs depend strongly on the neutron star equation of state (EOS) and for the more dominant f -modes these are thought to lie somewhere in the region of 1 to 4 kHz and 50 to 500 hundred ms, respectively. Andersson & Kokkotas [4] have shown how the mass and radius of a neutron star may be constrained by gravitational wave observations of the QNM frequencies and decay times. Conversely, if the EOS of the neutron star were known with some precision, it would be possible to compute the expected decay times and frequencies of the QNMs. This would provide a well constrained waveform model for aiding the identification of a potential gravitational wave signal following a neutron star ring-down. However, the behaviour of matter at the densities found in neutron stars is not well understood and there exist many different models for the neutron star EOS. It is, therefore, necessary to develop techniques which are robust to the uncertainties in these models.

While the gravitational wave emission from neutron star QNMs is expected to be weak (inducing typical strain amplitudes of $\sim 10^{-24}$), their detection is further hampered by the presence of instrumental glitches that can closely resemble short-duration gravitational wave signals.

In this work, we demonstrate the feasibility of applying Bayesian inference to the robust detection of neutron star

gravitational wave ring-downs through a process of model selection. We highlight how the methodology may be extended to include a more realistic range of glitches and developed into a multi-detector search.

II. PERTURBED NEUTRON STARS & ASTEROSEISMOLOGY

When the solid crust of a neutron star is severely disrupted or cracked, some of the stored elastic energy is channeled into the oscillatory modes of the star. Quadrupolar excitations will then be strongly damped by gravitational wave emission [1]. The different modes may be labelled according to the spherical harmonic indices l and m which describe the angular dependence and number of nodes.

The fundamental fluid mode, or f -mode (as first shown by Kelvin for the case of a non-rotating, uniform density star) has angular frequency

$$\omega_f^2 = \frac{2l(l-1)}{2l+1} \frac{GM}{R^3}, \quad (1)$$

where M and R are the stellar mass and radius, respectively. This is also a reasonable estimate for more realistic equations of state [5] and we see that, for non-radial modes with $l = 2$, the f -mode pulsations have frequencies ~ 2 kHz taking the fiducial values $M = 1.4M_{\odot}$ and $R = 10$ km. Other modes, such as the pressure (p) and space-time (w) modes, have considerably higher frequencies than this. Gravitational wave interferometers like GEO600 [6], LIGO [7] and VIRGO [8] are more sensitive at lower frequencies¹ making the f -mode the most favourable for a gravitational wave search. The

^{*}Electronic address: jclark@astro.gla.ac.uk

[†]Electronic address: siong@astro.gla.ac.uk

[‡]Electronic address: matthew@astro.gla.ac.uk

[§]Electronic address: graham@astro.gla.ac.uk

¹ Sensitivity curves for the LIGO and GEO600 interferometers can be found at http://www.ligo.caltech.edu/~jzweizig/distribution/LSC_Data and <http://www.geo600.uni-hannover.de/geocurves>, respectively.

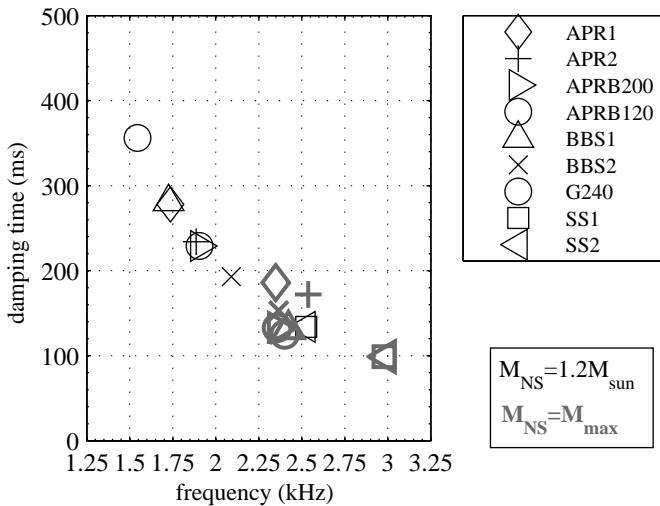


FIG. 1: The f -mode frequencies & damping times for the variety of different equations of state (indicated by symbol shape) and the extremal neutron star masses (indicated by colour and symbol weight) considered in [10].

ring-down timescale, τ_f , is given by the ratio of the oscillation energy to the total power emitted as gravitational waves [4]. This yields $\tau_f \sim R(R/M)^3$, where M and R are the mass and radius of the neutron star, respectively.

So, given some EOS, which defines the ratio M/R , it is possible to calculate the exact damping times and frequencies of the QNMs. Andersson & Kokkotas [4] do precisely this for a variety of equations of state and establish empirical relations for the f -mode damping time and frequency. On the other hand, we can consider the inverse problem and use gravitational wave observations of the f -mode frequency and damping time to constrain the neutron star EOS. Indeed, there has already been an attempt to use the electromagnetically observed frequencies of potential torsional mode oscillations in two SGRs to constrain their equations of state [9].

Here, our interest is in using what little *is* known about

the neutron star equation of state to inform us with regards to sensible gravitational wave waveforms to search for. Fig. 1 shows the results of calculations by Benhar *et al* [10] of the f -mode frequency and damping time, using several realistic EOSs and the extremal neutron star masses. M_{max} refers to the maximum neutron star mass allowed by the EOS. The reader is directed to [10] and the references therein for descriptions of the different equations of state.

Examining Fig. 1 we see that the equations of state considered in [10] yield typical f -mode frequencies of $\nu_f \sim 1.5 - 3$ kHz and damping timescales of $\tau_f \sim 50 - 400$ ms. Later, we use these ranges to set sensible limits of our priors for each parameter.

Gravitational wave emission

Following Thorne [1], we model the gravitational wave strain amplitude at the Earth from the n -th QNM as:

$$h(t) = \begin{cases} h_0 \sin(\omega_n(t - t_0)) \exp(-(t - t_0)/\tau_n) & \text{for } t \geq t_0 \\ 0 & \text{otherwise,} \end{cases} \quad (2)$$

where h_0 , ω_n and τ_n are the initial amplitude, angular frequency and characteristic damping time of the signal, and t_0 is the start time of the signal. We take $n = 0$ to represent the f -mode.

Furthermore, h_0 , ω_0 and τ are related to the total gravitational wave energy via the following relation [3],

$$E_{\text{GW}} = \frac{c^3 D^2}{4G} \left(h_0 \omega_0 \tau^{\frac{1}{2}} \right)^2, \quad (3)$$

where D is the distance to the source. We can, therefore, write down an expression for the the expected initial amplitude for f -mode ring-downs using fiducial parameter values:

$$h_0 \sim 5 \times 10^{-24} \left(\frac{E_{\text{GW}}}{10^{-11} M_{\odot} c^2} \right)^{1/2} \left(\frac{\tau}{200 \text{ ms}} \right)^{-1/2} \left(\frac{\nu_0}{2 \text{ kHz}} \right) \left(\frac{D}{15 \text{ kpc}} \right)^{-1}. \quad (4)$$

Search triggers & QNM excitation

There are several ways to generate stellar pulsations including close encounters with orbital companions and accretion (e.g., of comets), the ringing of proto-neutron stars following supernovae, soft γ -ray repeater (SGR) flaring activity and crustal disruption due to pulsar glitches.

Our aim is to search for gravitational waves from the latter two mechanisms. This is because both pulsar glitches and the SGRs provide an observable electromagnetic counterpart (which may be used to ‘trigger’ the search) and occur with a frequency making them practical for a triggered search. The most prolifically glitching pulsar, PSR J0537-6910, has a glitch rate of $\sim 4 \text{ year}^{-1}$ [11], whilst other regular glitchers like the Crab pulsar

and Vela have rates of order $\sim 0.5 \text{ year}^{-1}$ [12, 13]. SGRs are seen to emit bursts at rates of a few to 10 year^{-1} [14], whereas hyperflares are much rarer events occurring maybe once a decade. Other potential candidates seen to glitch are the anomalous X-ray pulsars (AXPs).

Pulsar glitches

Pulsar glitches are observed as sudden irregularities in the rotation rate of pulsars and are characterised by a step increase in rotation frequency. The characteristics of glitches vary between pulsars. For example, some show step changes in the spin-down rate and others exponential recoveries to pre-glitch parameters. The exact characteristics give clues to the underlying mechanisms causing the glitch.

The mechanisms responsible for pulsar glitches are still unclear, but there are two main candidates to explain the underlying process and some of the differences between glitches. For older pulsars it seems glitches are likely caused by a dramatic decoupling between the star's solid crust and superfluid interior [15]. Glitches in the young Crab pulsar are thought to be associated with a reconfiguration of the solid crust [16]: the spin-down reduces the centrifugal force and the crust reaches breaking strain. The ensuing relaxation of ellipticity will cause a sudden change in the moment of inertia, producing the observed glitch, and the crustal rupture will set up a starquake, hopefully causing f -mode excitations. The reality of the mechanism is likely to be very complex and may be a combination of the two.

For the two different glitch models the amount of energy released can be estimated in different ways as shown in van Riper *et al.* (1991) [17]. They assume all the energy released goes into heating the star, whereas we will make the assumption that it goes into exciting quasi-normal modes. For the angular momentum exchange model (thought to be the most probable explanation for the Vela pulsar glitches) the amount of energy released depends on the angular momentum exchanged between the superfluid interior and crust $\Delta J \sim I\Delta\Omega$, where $\Delta\Omega$ is the angular frequency change from the glitch. The energy change is then $\Delta E = \Delta J\Omega_{\text{lag}}$, where Ω_{lag} is the lag frequency between the superfluid and crust, with an estimated range of values of $1\text{-}100 \text{ rads}^{-1}$ (or possibly $\lesssim 0.1 \text{ rads}^{-1}$) [17]. For the largest Vela pulsar glitch, with a fractional frequency change of $\Delta\Omega/\Omega = 3.1 \times 10^{-6}$ [18], this gives a $\Delta J \sim 2 \times 10^{34} \text{ J}$ giving an energy release of $\Delta E \sim 10^{-13} - 10^{-11} M_{\odot} c^2$ for the range $\Omega_{\text{lag}} \approx 1\text{-}100 \text{ rads}^{-1}$.

For starquake driven glitches the energy released is given in Ref. [17] as $\Delta E \approx \mu V_{\text{crust}} \epsilon_{\text{max}} \epsilon_{\text{quake}}$, where $\epsilon_{\text{quake}} = \Delta\Omega/\Omega$ is equivalent to the relative change in moment of inertia, μ is the mean shear modulus of the star, V_{crust} is the volume of the crust (where $\mu V_{\text{crust}} \sim 10^{41} \text{ J}$), and ϵ_{max} is the maximum deformation from equilibrium the crust can withstand without breaking (given

in Ref. [17] as $\epsilon_{\text{max}} \lesssim 10^{-2}$ although this could vary somewhat). Assuming this ϵ_{max} and taking the largest Crab pulsar glitch, where $\Delta\Omega/\Omega \sim 8 \times 10^{-8}$ [19], we get an energy release of $\Delta E \sim 5 \times 10^{-16} M_{\odot} c^2$. If the starquake mechanism can provide similar fractional frequency changes to a neutron star to those seen in the Vela pulsar during glitches, then this mechanism could still be a valuable potential source.

Soft γ -ray repeater flares

Soft γ -ray repeaters are high energy transient sources with typical photon energies of $10 - 30 \text{ keV}$ and similar burst characteristics from one event to the next, although they are also seen as quiescent X-ray sources. These objects are identified as highly magnetised ($B \approx 10^{14} \text{ Gauss}$) neutron stars, or 'magnetars'. They are occasionally seen to emit giant flares, or hyper-flares, which have thousands of times the luminosity, and harder spectra, than the regular bursts. The hyperflares are thought to occur when magnetic field becomes twisted and causes a catastrophic reconnection, inducing tectonic activity. The field annihilation/reconnection in seismic faults is responsible for the observed γ -ray emission and, again, we expect the crustal disruption to excite the QNMs of the magnetar [20].

Before moving on to describe the search in detail, we outline some ideas behind Bayesian model selection.

III. BAYESIAN MODEL SELECTION

Bayes' theorem describes how to assign a posterior probability to some parameterised model M_i , given a set of data or observations D and some background information I which determines the hypothesis space $\{M_i\}$:

$$p(M_i|D, I) = \frac{p(M_i|I)p(D|M_i, I)}{p(D|I)}. \quad (5)$$

Here $p(D|M_i, I)$ is the *marginal likelihood* or *evidence* and represents the influence of the data on our belief in M_i ²; $p(M_i|I)$ is the *prior* probability of model M_i and describes our state of belief in M_i , preceding examination of the data D ; $p(D|I)$ ensures that the posterior is correctly normalised.

Our desire here is to detect a gravitational wave of a known shape (see Eq. 2) but with unknown parameters within some range in noisy data. The obvious question we might ask is, 'does this data contain a ring-down

² The name *marginal likelihood* reflects the fact that we have marginalised over the parameter values that are associated with M_i .

gravitational wave?’. We denote the data by D and the gravitational waveform model by M_{GW} .

The posterior probability $p(M_i|D, I)$ then tells us the degree of belief to assign to the model M_i . To properly normalise the posterior, however, we must marginalise over the entire hypothesis space:

$$p(D|I) = \sum_i p(M_i|I)p(D|M_i, I). \quad (6)$$

If the system is sufficiently well understood, it is possible to enumerate all possible models M_i and the posterior probability of any one model can be calculated directly from Bayes theorem. However, this cannot always be done and it often makes more sense to evaluate the probability of one model relative to another. Such comparisons are performed via the *odds ratio*:

$$O_{12} = \frac{p(M_1|D, I)}{p(M_2|D, I)}. \quad (7)$$

For a gravitational wave search we might choose M_1 to be the proposition that the noisy data contains a gravitational wave, and M_2 to be the proposition that the data only contains detector noise.

Substituting the right hand side of Bayes’ theorem for the posteriors in Eq. 7, we see that the normalisation term $p(D|I)$ drops out and we are left with

$$O_{12} = \frac{p(M_1|I) p(D|M_1, I)}{p(M_2|I) p(D|M_2, I)}. \quad (8)$$

The first term, the prior odds, is the ratio of the prior probabilities for each model. Typically, we assume complete naivete and set the prior odds equal to unity. The second term is the ratio of the evidences from each model and is called the Bayes factor. Clearly a large value of the Bayes factor indicates a strong preference for M_1 .

The evidence is computed by integrating the likelihood $p(D|\boldsymbol{\theta}, M_i, I)$ over all model parameters $\boldsymbol{\theta}$ and weighting by the prior on those parameters, $p(\boldsymbol{\theta}|I)$, leading to the alternative name ‘marginal likelihood’:

$$p(D|M_i, I) = \int_{\boldsymbol{\theta}} p(\boldsymbol{\theta}|M_i, I)p(D|\boldsymbol{\theta}, M_i, I)d\boldsymbol{\theta}. \quad (9)$$

So given some competing models M_1 and M_2 , we can evaluate the evidences $p(D|M_1, I)$, $p(D|M_2, I)$ and assuming prior odds of unity, use the odds ratio to decide which is most likely, given the data D .

A. Application & choice of models

Here, ‘model’ shall refer to a *class* of descriptions for the data. An example is ‘the data contains a ring-down

gravitational wave signal in addition to noise’. Note that we have defined the generic shape of the data (a noisy ring-down) but not any parameter values. A particular signal with a specified set of parameter values is called a ‘template’. In this way, a model defines a set of templates with parameter values determined by the priors in that model. Additionally, when we talk about the ‘evidence for the model’, we are referring to the marginal likelihood for that model, i.e., $p(D|M, I)$. The total evidence of the hypothesis space $p(D|I)$ is eliminated through the use of the odds ratio.

M_1 : Ring-down waveform \mathcal{E} Gaussian white noise

The expression for the ring-down waveform $h(t)$ is given by Eq. 2. We assume that the noise $n(t)$ is white and Gaussian over a sufficiently broad band and that the data stream is given by

$$d(t) = h(t) + n(t), \quad (10)$$

where the noise $n(t)$ has zero mean and variance σ_n^2 . However, to simplify data conditioning, we work with the power spectral density,

$$D(\omega) = |\tilde{h}(\omega)|^2 + |\tilde{n}(\omega)|^2 + 2|\tilde{h}(\omega)\tilde{n}(\omega)|, \quad (11)$$

where $\tilde{h}(\omega)$ is the Fourier transform of $h(t)$,

$$\tilde{h}(\omega) = \frac{h_0\tau}{\sqrt{1 + (\omega - \omega_0)^2\tau^2}}, \quad (12)$$

so that our parameter space is given by $\boldsymbol{\theta} = \{h_0, \omega_0, \tau\}$. Notice that working with the power spectral density has the effect of pre-marginalising over the start time of the signal, t_0 with a uniform prior. The power spectral density is estimated from fast Fourier transforms (FFTs) of consecutive segments of the time series. This yields a spectrogram with time bins indexed by i and frequency bins indexed by j .

The likelihood of obtaining power D_{ij} in the i -th time bin at the j -th frequency (i.e., the i, j -th pixel), given a template with signal power $S_{ij} = |\tilde{h}(\omega_j)|^2$ is a non-central χ^2 distribution with two degrees of freedom and non-centrality parameter equal to the power from the template, i.e.

$$p(D_{ij}|S_{ij}, M_1, I) = \frac{1}{2\sigma_{ij}^2} \exp\left\{-\frac{D_{ij} + S_{ij}}{2\sigma_{ij}^2}\right\} I_0\left(\frac{\sqrt{D_{ij}S_{ij}}}{\sigma_{ij}^2}\right), \quad (13)$$

where σ_{ij}^2 is the variance of the Fourier components in that pixel and I_0 is the zeroth order modified Bessel function of the first kind. If the data is Gaussian and white, the power spectral density can be normalised such that the Fourier components follow Gaussian distributions with zero mean and unity variance (i.e., $\sigma_{ij}^2 = 1$).

To calculate a single odds ratio in each time bin, we require the joint probability across frequencies,

$$p(\{D\}|\boldsymbol{\theta}, M_1, I) = \prod_j p(D_j|\boldsymbol{\theta}, M_1, I), \quad (14)$$

where we have dropped the time bin index i for notational convenience. Finally, we adopt independent, uniform priors on the parameters $\boldsymbol{\theta} = \{h_0, \omega_0, \tau\}$ with ranges on ω_0 and τ based loosely on the expected values in the literature. For the amplitude h_0 , however, there is little to be gained by restricting the prior range and the prior on h_0 is taken to run from zero to some arbitrarily high value. The joint prior is then

$$p(\boldsymbol{\theta}|M_1, I) = p(h_0|M_1, I)p(\omega_0|M_1, I)p(\tau|M_1, I) \quad (15)$$

where

$$p(\theta|M_1, I) = \begin{cases} \frac{1}{\theta_{\max} - \theta_{\min}} & \text{for } \theta_{\min} \leq \theta \leq \theta_{\max} \\ 0 & \text{otherwise,} \end{cases} \quad (16)$$

and θ is any one of the parameters in model 1.

M₂: Gaussian white noise only

M_2 is our null detection hypothesis: the data is modelled as white Gaussian noise, without any gravitational wave signal, so that $d(t) = n(t)$. Again, we work in terms of the power in each spectrogram pixel D_{ij} . If the spectrogram has been normalised such that the individual Fourier components are normally distributed with mean zero and variance of unity, we know that the power in the j -th frequency bin follows a central χ^2 distribution with two degrees of freedom,

$$p(D_{ij}|M_2, I) = \frac{1}{2\sigma_j^2} \exp\left\{-\frac{D_{ij}}{2\sigma_j^2}\right\}, \quad (17)$$

where σ_j^2 is the variance of the Fourier components in the j -th frequency bin. If it is possible to estimate the variance in each frequency bin (from an off-source piece of data, for example), then the result is also valid for

coloured noise.

Notice that we have arrived at the evidence from M_2 without making any mention of parameterisation, priors or marginalisation. This can also be derived in a purely Bayesian context by considering the likelihood of a pixel power D_{ij} , given a template power S_{ij} (Eq. 13). In the case of a model where there is no contribution to the power from a gravitational wave, we know *a priori* that $S_{ij} = 0$. That is to say

$$p(S_{ij}|M_2, I) = \delta(S_{ij}), \quad (18)$$

where δ is the Dirac delta function. If we now marginalise the likelihood given by Eq. 13 over power using this prior, we arrive at Eq. 17.

Thresholding O_{12}

O_{12} is the ratio of the posterior probabilities for each model, so it might seem sensible to choose $O_{12} > 1$ to indicate a preference for M_1 over M_2 . While this is true, such a threshold for gravitational wave detection neglects the role of our prior odds and the need for an acceptable false alarm rate.

By setting the prior odds equal to unity, we are saying we believe *a priori* that both models are equally probable. Even if we truly were that ignorant, the influence of the data through the Bayes factor will mean that the odds generally fluctuate around some mean value far from unity. Instead, we search for excesses from the mean ‘off-source’ (zero-signal) odds to indicate a preference for our gravitational wave model. Alternatively, it would be straightforward to estimate the prior odds using an off-source sample. The value of the prior odds could then be chosen such that an odds ratio of unity corresponds to a false detection probability of 0.5. Ultimately, the odds threshold, denoted O_{thresh} , can be set according to the results of large numbers of trials and so the overall normalisation is relatively unimportant.

Finally, the magnitude of the exponential and Bessel functions which occur in the likelihood mean that it is convenient to work with the natural logarithm of the odds ratios and evidences. For clarity then, $\log_e O_{12}$ refers to the natural logarithm of the odds ratio between models M_1 and M_2 .

B. Algorithm & example

We now consider an example using data synthesised in Matlab³ to illustrate the above principles. First, the outline of the algorithm is as follows:

1. Estimate the variance of the noise using some stretch of data away from the time of an expected gravitational wave signal (i.e., *off-source*).
2. Construct the power spectral density of discrete time segments of data centred around the expected gravitational wave signal (i.e., *on-source*) to create a time-frequency map of power (spectrogram).
3. Normalise the power spectral density so that, in the absence of a signal in the data, the power in a given frequency bin follows a central χ^2 distribution with two degrees of freedom.
4. Compute the evidences $p(D|M_1, I)$, $p(D|M_2, I)$ for each model in each spectrogram time bin.
5. Assuming prior odds of unity, evaluate the odds ratio O_{12} in each time bin. An excess in the odds ratio indicates a preference for M_1 and, therefore, a potential detection.

To characterise the signals used to test the algorithm, we define the signal-to-noise ratio as

$$\rho^2 = \int_{-\infty}^{+\infty} \frac{|h(\nu)|^2}{S(\nu)} d\nu, \quad (19)$$

where $S(\nu)$ is the one-sided noise spectral density. In the case of Gaussian white noise, $S(\nu)$ is given by

$$S(\nu) = 2 \frac{\sigma_n^2}{f_s} \forall \nu, \quad (20)$$

where σ_n^2 is the variance of the time series data and f_s is the sampling frequency. It is also useful to define the root-sum-squared amplitude

$$h_{\text{rss}} = \left(\int_{-\infty}^{+\infty} |h(t)|^2 dt \right)^{1/2}. \quad (21)$$

To demonstrate the operation of the algorithm, we inject a ring-down signal into 100s of Gaussian white noise with amplitude spectral density $10^{-22} \text{ Hz}^{-1/2}$. To investigate the response to a typical instrumental glitch which closely resembles our target waveform, we also inject a sine-Gaussian signal of the form

$$h(t) = h_0 \sin(\omega(t - t_0)) \exp\{-(t - t_0)^2/\tau\}, \quad (22)$$

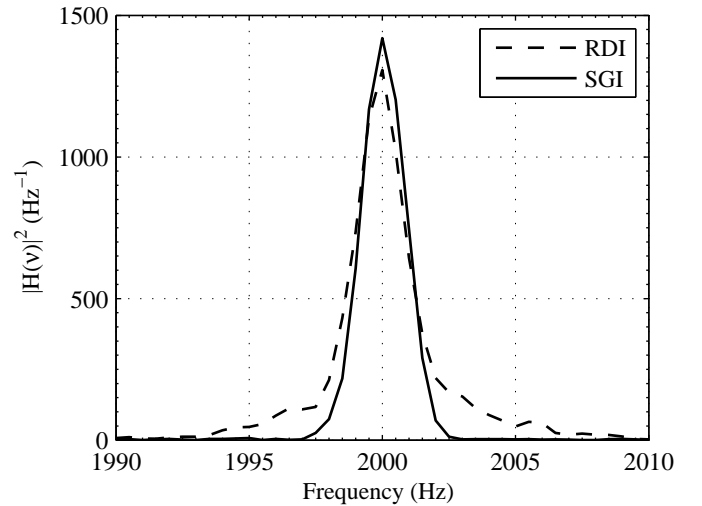


FIG. 2: The normalised power spectral densities of the ring-down (RDI, dashed line) and sine-Gaussian (SGI, solid line) injections.

Injection	Parameter	Value
RDI	Injection time	t_0 10s
	Initial amplitude	h_0 200×10^{-22}
	Central frequency	ν_0 2 000 Hz
	Decay time	τ 0.2 s
	SNR	ρ 40.5
SGI	Injection time	t_0 80 s
	Initial amplitude	h_0 106×10^{-22}
	Central frequency	ν_0 2 000 Hz
	Decay time	τ 0.2 s
	SNR	ρ 40.4

TABLE I: Injected signal parameter values.

where, h_0 is the maximum amplitude of the signal, ω is the angular frequency and τ is the decay time. Table I shows the parameter values used to generate the injections and Fig. 2 shows the power spectral density of each signal, calculated from the noisy data and normalised so that the noise follows a central χ^2 distribution. It is the job of the algorithm to detect and differentiate between these two signals, only producing a candidate detection when the ring-down is present. The prior ranges used for each parameter are shown in Table II.

Fig. 3 shows the odds ratio in each spectrogram time bin. The ring-down injection at $t = 10$ s is strongly detected. Notice, however, that the sine-Gaussian we have injected to mimic an unwanted instrumental glitch is also detected

³ <http://www.mathworks.com/products/matlab>

Parameter	Lower Limit	Upper Limit
h_0	0	500×10^{-22}
ν_0	1 500 Hz	3 000 Hz
τ	0.05 s	0.5 s

TABLE II: Parameter prior ranges. The prior distributions are taken as uniform over these ranges.

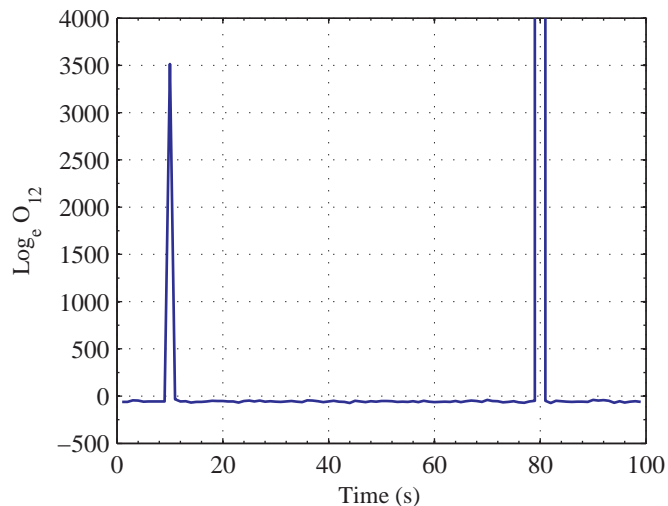


FIG. 3: The log-odds in favour of a ring-down plus noise, versus the possibility that the power is due to noise alone. The first peak corresponds to the ring-down injection, the second to the sine-Gaussian injection.

with an odds ratio higher than that for the ring-down injection.

This is not because the injected sine-Gaussian matches the ring-down template more closely than the injected ring-down signal does. Instead, it is because the power contained in the sine-Gaussian is distributed over a narrower bandwidth and has a higher peak amplitude. The result is that the evidence for the noise model, M_2 , is much smaller than it is in the presence of the ring-down injection where the power is more spread out. Since the noise model evidence appears in the denominator, the odds ratio O_{12} is correspondingly higher for the sine-Gaussian than it is for the ring-down. To address this issue, we make a straightforward extension to the odds ratio to consider multiple hypotheses.

C. Multiple hypothesis extension

To handle the possibility of sine-Gaussian instrumental glitches, we rewrite the posterior in the denominator as the sum of the probability of the noise model M_2 and a

model for sine-Gaussian glitches, M_3 . This gives

$$p(M_-|D, I) = p(M_2|D, I) + p(M_3|D, I) + \dots, \quad (23)$$

where M_- denotes the proposition that the data does not contain a ring-down gravitational wave and the ellipsis is to emphasise the fact that this null-detection hypothesis M_- may be further extended to include additional models for instrumental glitches. Similarly,

$$p(M_+|D, I) = p(M_1|D, I) + \dots, \quad (24)$$

where, again, it is straightforward to include additional signal models if desired. The result is that we are left with a comparison of the probability in favour of a gravitational wave with the probability of an instrumental glitch or that of the noise model, thus making maximal use of any knowledge we might have regarding transient features in the data.

Using M_- now as the alternative hypothesis, we obtain a new odds ratio O_{123} :

$$O_{123} = \frac{p(M_1|D, I)}{p(M_2|D, I) + p(M_3|D, I)}. \quad (25)$$

Assuming the prior on each model is identical, the posterior probabilities in O_{123} may be replaced by the evidences $p(D|M_i, I)$ for $i = 1, 2, 3$. Fig. 4 shows the result of using this new expression for the odds ratio and the same data from the previous example. Since the parameterisation for the sine-Gaussian is identical to that of the ring-down, the priors in table II are also used to evaluate $p(M_3|D, I)$. There is no fundamental reason for using the same prior ranges for both models. Indeed, a realistic application would most likely have very different priors for the parameters in different models even if the parameterisation was the same. Here, the priors in Table II are used for both M_1 and M_3 for computational simplicity.

The incorporation of the alternative model eliminates the previous problem of detecting sine-Gaussian signals with high odds ratios. Also note that the size of the peak indicating the ring-down has diminished quite substantially but is still clearly visible above the background. This reduction is due to a non-zero contribution from $p(M_3|D, I)$ in the denominator of O_{123} . Unless they are mutually exclusive in some way, the inclusion of additional models in the denominator of the odds ratio will generally increase the robustness of the search, at the cost of sensitivity.

IV. PERFORMANCE

We now investigate the performance of the algorithm by considering both formulations of the odds ratio, comparing the relative merits of each.

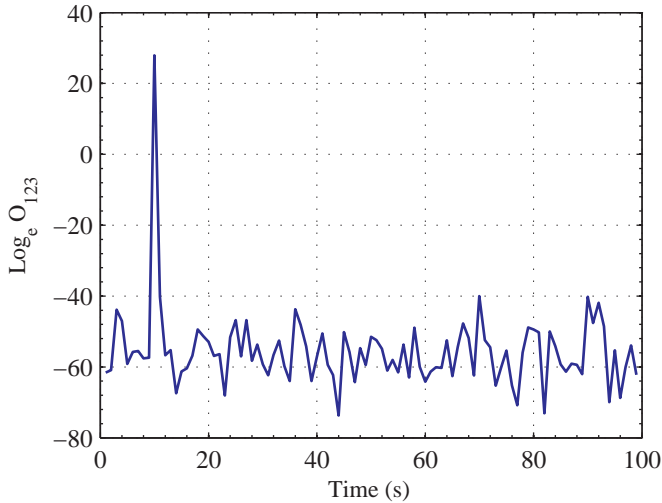


FIG. 4: The log-odds in favour of a ring-down plus noise, versus the possibility that the power is due to noise alone *or* a sine-Gaussian glitch. The second (sine-Gaussian) peak seen in Fig. 3 is no longer present.

A ‘false alarm’ is defined as any unwanted transient event which causes the odds ratio to cross the threshold and generate a candidate detection. For white noise, false alarms are caused by spikes in the noise amplitude. The false alarm probability is calculated from the fraction of time bins in a large sample for which the odds ratio crosses the threshold when there is no ring-down signal present.

We investigate the response to ‘off-source’ data (i.e., white noise with no injections) by combining the results of ten 500 s spectrograms with a 1 s time resolution to give 5 000 off-source time bins. To evaluate the sensitivity of the search, ring-down signals of a constant signal-to-noise ratio are injected every other second into 500 second segments of white noise, synthesised in Matlab. This is then used to construct a 500 s spectrogram with 1 s time-resolution and 0.5 Hz frequency resolution for each set of injections, leading to 250 signal injections for each value of the signal-to-noise ratio. The fact that there are spectrogram time bins with no signal injection helps to prevent contamination from adjacent bins. We vary the signal-to-noise ratio through the value of h_0 only and always compare signals of equal bandwidth and at the same frequency, each of which are held constant at 2 kHz and 200 ms, respectively. The noise amplitude spectral density is $10^{-22} \text{ Hz}^{-1/2}$, representative of the LIGO noise floor at these frequencies.

When we make use of the glitch catalogue in the expanded odds ratio O_{123} the objective is to be robust against unwanted glitches as well as spurious noise effects. Therefore, we also define a false alarm probability due to sine-Gaussians. This is found in exactly the same way as the sensitivity to ring-downs but using sine-Gaussian injections. The false alarm probability due to sine-Gaussians, therefore, is simply the fraction of the

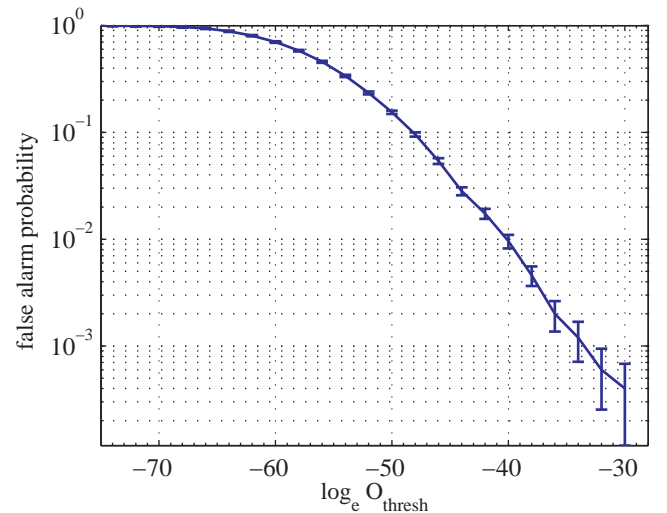


FIG. 5: The false alarm probabilities in Gaussian white noise for different $\log_e O_{12}$ thresholds. Error bars represent 1σ Poissonian errors.

250 injected sine-Gaussians which cause the odds ratio to exceed the threshold.

A. O_{12} : ring-down vs noise

We take our desired false alarm probability here to be 1%. Fig. 5 shows the false alarm probability as a function of the log odds ratio threshold, $\log_e O_{\text{thresh}}$, and we see that a false alarm probability of 1% is given by $\log_e O_{\text{thresh}} = -40$.

Fig. 6 shows *receiver operating characteristic* (ROC) curves for O_{12} . ROC curves are plots of sensitivity (the probability of detecting what we are looking for) as a function of false alarm probability (the probability of claiming a detection due to a spurious noise event or instrumental glitch) for a given strength signal. The different false alarm probabilities correspond to different values of the detection threshold, O_{thresh} , and are found by reading the appropriate values from Fig. 5. When there are no injected signals, the only events to cause the odds ratio to cross the threshold are false alarms and the false alarm probability should be equal to the detection probability.

Although the ROC curves give some indication of how the sensitivity varies with injected signal strength, it is also helpful to examine efficiency curves, where the fraction of detected ring-downs is plotted against the injected signal strength, for a given threshold. Fig. 7 shows the detection efficiency using $\log_e O_{\text{thresh}} = -40$ with corresponding false alarm probability of 1%.

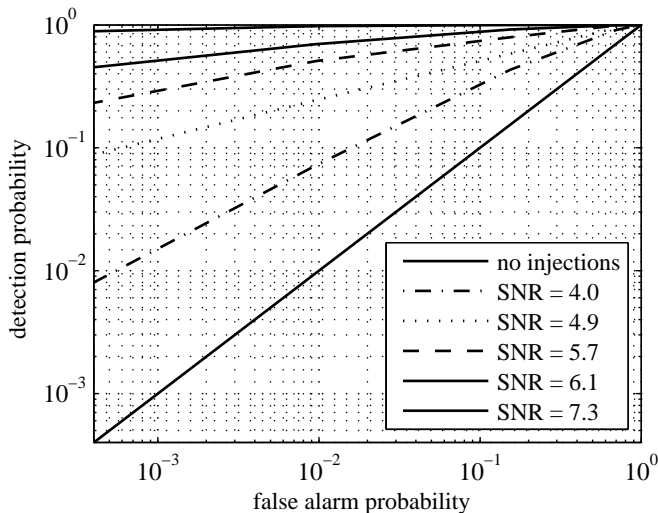


FIG. 6: Receiver operating characteristic curves for O_{12} . False alarm probabilities are those from amplitude fluctuations in Gaussian white noise.

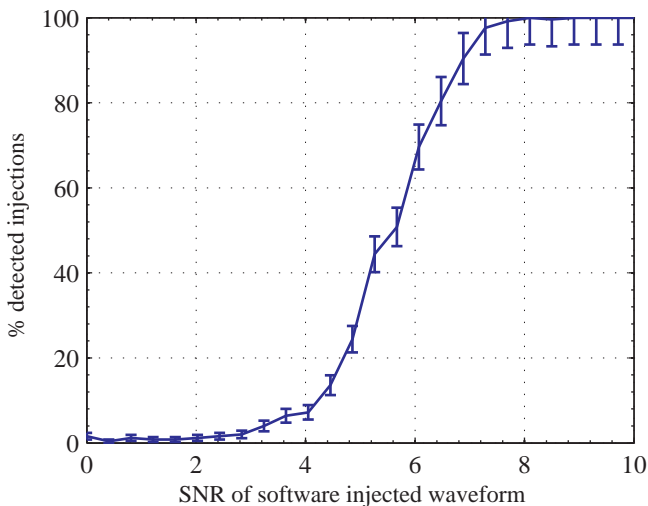


FIG. 7: The detection efficiency obtained for $\log_e O_{12}$ using a threshold $\log_e O_{\text{thresh}} = -40$. Error bars represent 1σ Poissonian errors.

The algorithm's performance is best summarised by the signal-to-noise ratio required to give a detection probability of 50% while maintaining the desired false alarm probability. A signal-to-noise ratio $\rho = 5.5$ is required for 50% ring-down detection, corresponding to an initial ring-down amplitude at Earth of $h_0 = 2.7 \times 10^{-21}$ at current LIGO sensitivities.

Equation 3 on page 2 relates h_0 to the distance to the source and the energy emitted as gravitational waves. Using this equation and assuming the fiducial distance of 15 kpc, the energy required to generate this initial ring-down amplitude at the earth is $2.8 \times 10^{-5} M_{\odot} c^2$. Conversely, when we assume the fiducial energy in grav-

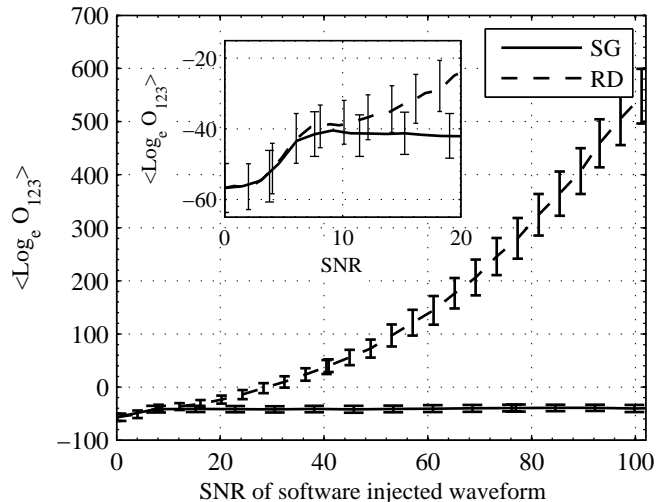


FIG. 8: The mean value of $\log_e O_{123}$ for varying strengths of signal-to-noise ratio. Results of ring-down injections are shown by the dashed curve, while the solid curve shows the results of the sine-Gaussian injections. Error bars represent 1σ dispersion. *Inset*: exploded view of $\langle \log_e O_{123} \rangle$ for low signal-to-noise ratio injections.

itational waves of $10^{-11} M_{\odot}$, the distance to the source must be 8.9 pc for this amplitude. These results are summarised in table III on page 12.

B. O_{123} : Ring-down vs noise or sine-Gaussian glitch

We now evaluate the performance of the algorithm using the more robust comparison between ring-downs, white noise and sine-Gaussians. Again, we begin by examining the false alarm probability in Gaussian white noise. In the absence of anything resembling a sine-Gaussian our new odds ratio O_{123} has no significant contribution from the sine-Gaussian evidence and tends towards the original comparison between ring-downs and white noise. i.e.,

$$\lim_{p(D|M_3, I) \rightarrow 0} \{O_{123}\} = O_{12}, \quad (26)$$

meaning that, for the case of Gaussian white noise, both O_{12} and O_{123} have the same false alarm probabilities.

The response of O_{123} to sine-Gaussians is compared with the response to ring-down injections in Fig. 8. The horizontal axis shows the signal-to-noise ratio of each type of injected signal (ring-down or sine-Gaussian) and the vertical axis gives the mean value of $\log_e O_{123}$, calculated from 250 injections of each signal type. The response can be separated into three distinct regions of signal-to-noise ratio, ρ :

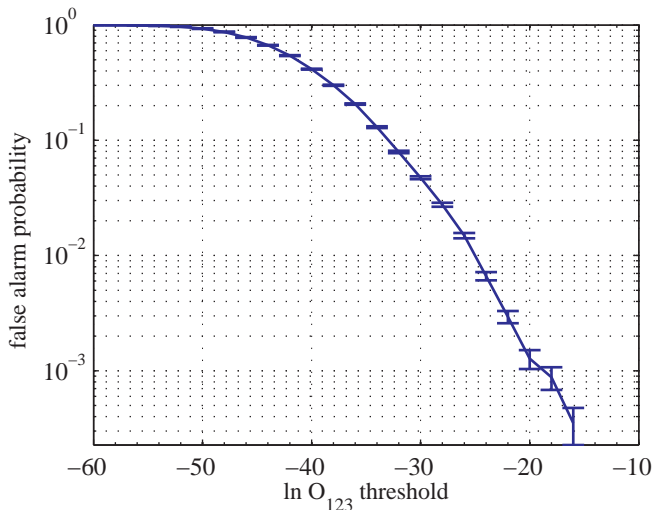


FIG. 9: The false alarm probabilities and corresponding $\log_e O_{123}$ thresholds from sine-Gaussians with signal-to-noise $\rho \geq 6$. Error bars represent 1σ Poissonian errors.

$\rho \lesssim 2$: there is effectively no response to sine-Gaussians or ring-downs and any signal present is indistinguishable from noise.

$2 \lesssim \rho \lesssim 6$: the response to sine-Gaussians and ring-downs is much the same. All we observe is that there is some excess in the odds ratio, compared to the value obtained for no injections. In this region, the evidence for sine-Gaussians and ring-downs is largely the same. The noise model evidence, however, will change dramatically in the presence of injected waveforms so that the denominator decreases and the value of the odds ratio increases.

$\rho \gtrsim 6$: the odds in favour of a ring-down begin to grow for the ring-down injections, while it appears to flatten out for the sine-Gaussian injections.

This plateau in the response can be used to estimate the maximum probability that the algorithm will mistake any sine-Gaussian for a ring-down for a given threshold. We assume that the mean and variance of the odds ratio for all sine-Gaussian injections reaches a maximum and remains approximately constant for signal-to-noise $6 < \rho < 120$ (for sine-Gaussians with $\rho > 120$, the odds in favour of a ring-down rapidly fall to zero).

We then collate the values of the odds ratios for all sine-Gaussian injections with $\rho \gtrsim 6$ and compute the false alarm probability for each threshold value. It can be seen from Fig. 9 that the original value $\log_e O_{\text{thresh}} = -40$ corresponds to a false alarm probability of 45% when the data contains a sine-Gaussian. This might seem like an unacceptably high false alarm rate for sine-Gaussians but there are two important points to note:

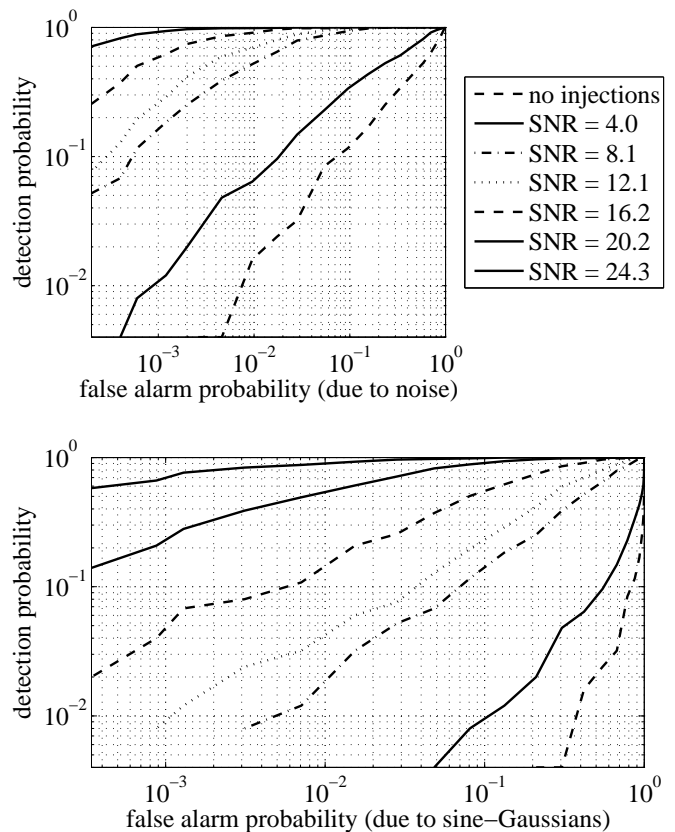


FIG. 10: Receiver operating characteristic curves for O_{123} . *Top panel*: ROC curve with false alarm probabilities due to spurious noise events. *Bottom panel*: ROC curve with false alarm probabilities due to sine-Gaussian glitches.

- a) this assumes the presence of sine-Gaussian glitches *a priori*. While this is an appropriate assumption for Gaussian white noise, we do not have a population model for the sine-Gaussian glitches. A more informative estimate of the probability of mistakenly detecting a sine-Gaussian glitch should fold in the effects of such a population model, through the prior on M_3 . In this work, we are more interested in demonstrating the inherent ability of the algorithm to discriminate between similar waveforms and this will not be considered.
- b) Only sine-Gaussians with signal-to-noise ratios $6 \leq \rho \leq 120$ generate an approximately constant response. Outside of this range, the value of the odds ratio drops off rapidly so that the 45% false alarm probability should be regarded as an approximate upper limit.

We use the threshold required to give a false alarm probability of 1% in white noise and state the corresponding probability of falsely identifying a sine-Gaussian as a ring-down *assuming there is one present*.

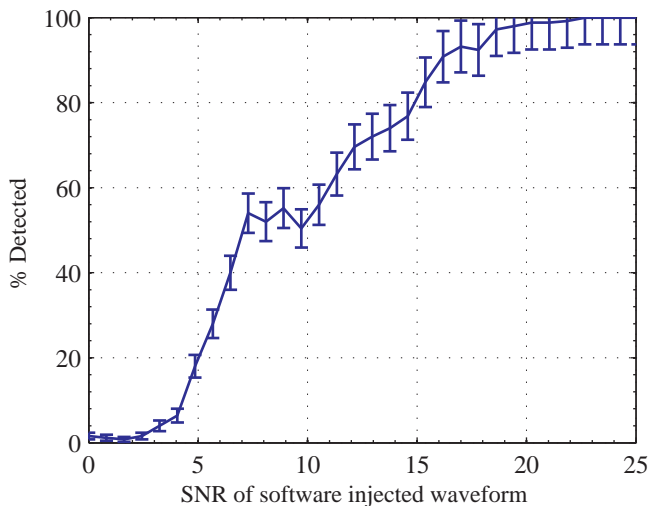


FIG. 11: The detection efficiency obtained for $\log_e O_{123}$ using a threshold $\log_e O_{\text{thresh}} = -40$. Error bars represent 1σ Poissonian errors.

Because we have two possible sources of false alarms, sine-Gaussians and noise events, we produce ROC figures for each, shown in each of the panels of Fig. 10. Notice from the bottom panel of Fig. 10 that setting the threshold according to the sine-Gaussian false alarm probability results in much lower detection probabilities. Rather, the point here is that we know that the algorithm responds more or less equally to the majority of sine-Gaussians and we are able to make statements regarding the probability of detecting *any* sine-Gaussian.

For comparison with the sensitivity of O_{12} , Fig. 11 shows the detection efficiency for O_{123} . The shape of this efficiency curve might seem a little confusing at first. Closer inspection reveals that the structure present corresponds to the different regions of Fig. 8 discussed on page 9. Specifically, the plateau in the efficiency curve corresponds to a similar plateau visible in the inset to Fig. 8, for $6 \lesssim \rho \lesssim 10$ where the value of $\log_e O_{123}$ remains approximately constant for all signals. We see that the signal-to-noise ratio required for 50% detection efficiency and 1% false alarm probability in Gaussian white noise is $\rho^{50\%} = 7.0$.

Again, it is important to consider these results in an astrophysical context. With the noise amplitude spectral density used for these investigations ($10^{-22} \text{ Hz}^{-1/2}$), a ring-down signal-to-noise ratio $\rho = 7.0$ corresponds to an initial amplitude $h_0 \sim 3.5 \times 10^{-21} \text{ Hz}^{-1/2}$. The gravitational wave energy required to produce a ring-down signal with 50% detection probability at the Earth with this amplitude is $4.6 \times 10^{-5} M_\odot c^2$ for a source at 15 kpc. Similarly, if we assume that $10^{-11} M_\odot c^2$ is emitted as gravitational waves, the source must lie at 6.9 pc. These results are summarised and compared with those from O_{12} in table III on page 12.

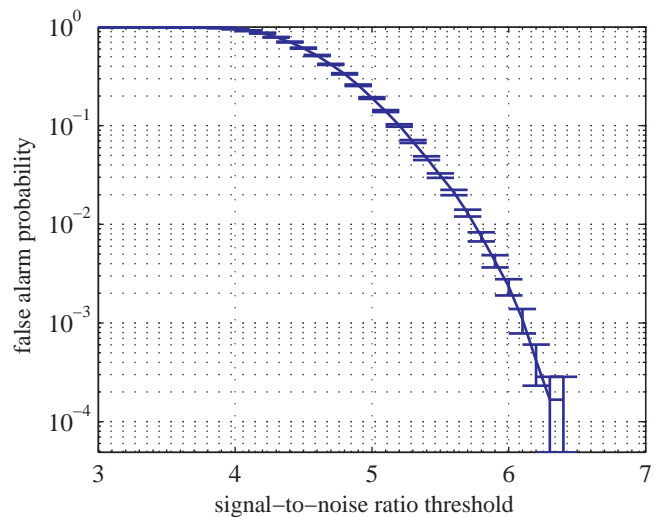


FIG. 12: The cumulative percentage of triggers produced by a matched filter based ring-down signal search code over a range of signal-to-noise ratios for data consisting of simulated Gaussian white noise.

C. Comparison to matched filtering

The LIGO Algorithm Library (LAL) and LALapps [21] software repositories used for much of the gravitational wave data analysis within the LIGO Scientific Collaboration (LSC)⁴ contain software for performing a matched filter based search for ring-down signals. Currently this is being used to search for ring-downs from perturbed black holes [22]. The software can be used to compare the false alarm probability of the matched filtering method with our method by running it on simulated white noise for the range of parameters given in Table II⁵. The template bank for the matched filtering was produced to give a maximum mismatch between adjacent template of 10%.

We define the false alarm probability to be the fraction of detection candidates generated by the algorithm whose signal-to-noise ratio crosses a given threshold. Fig. 12 shows the false alarm probability as a function of signal-to-noise ratio threshold: for a false alarm probability of 1%, we require a signal-to-noise ratio threshold of 5.75. The efficiency curve in Fig. 7 shows that this matched-filtering threshold agrees to within 1σ with the signal-to-noise ratio required for 50% detection efficiency when we use the odds ratio O_{12}

⁴ <http://www.ligo.org>

⁵ The matched filtering code defines the ring-down in terms of frequency and quality factor, Q , where $Q = f\tau/2\pi$.

Parameter	Symbol	Value Using O_{12}	Value Using O_{123}
Log odds threshold	$\log_e O_{\text{thresh}}$	-40	-40
False alarm probability (due to noise)	$p(- N)$	1%	1%
False alarm probability (due to sine-Gaussians)	$p(- SG)$	-	45%
Signal-to-noise	$\rho^{50\%}$	5.5	7.0
Initial strain amplitude	$h_0^{50\%}$	2.7×10^{-21}	3.5×10^{-21}
GW Energy	$E_{\text{GW}}^{50\%}$	$2.8 \times 10^{-5} M_{\odot} c^2$	$4.6 \times 10^{-5} M_{\odot} c^2$
Range	$D_{\text{GW}}^{50\%}$	8.9 pc	6.9 pc
Root-sum-squared strain	$h_{\text{rss}}^{50\%}$	6.03×10^{-22}	7.71×10^{-22}

TABLE III: Simulated sensitivity estimates for 50% detection efficiency and corresponding false alarm probabilities. $p(-|N)$ is the probability of a false alarm from white noise for the given threshold $\log_e O_{\text{thresh}}$. Similarly, $p(-|SG)$ is the probability of a false alarm given a sine-Gaussian event. All estimates assume a ring-down frequency $\nu = 2$ kHz, decay timescale $\tau = 200$ ms and a noise amplitude spectral density $10^{-22} \text{ Hz}^{-1/2}$. $E_{\text{GW}}^{50\%}$ is calculated for a distance $D = 15$ kpc and $D_{\text{GW}}^{50\%}$ is calculated for an energy in gravitational waves of $10^{-11} M_{\odot} c^2$.

V. FURTHER EXTENSIONS

We now highlight some outstanding issues and possible important extensions to this work which may be required to make the transition from ‘proof-of-concept’ to a useful search tool. Particularly, we address the issues of constructing the catalogue of alternative hypotheses, the extension to a multi-detector analysis and the outline for a full analysis pipeline.

Glitch classification

It is likely that the inclusion of extra information regarding glitches will increase robustness against instrumental transients which would otherwise generate a candidate detection event. For this to be effective, we require some classification scheme for these instrumental glitches which would allow the construction of a catalogue of glitch models as well as their associated priors.

Essentially, what is required is an automated pattern recognition tool which could be ‘trained’ on off-source interferometer data and used to generate a generic library of transient features. Fortunately, such techniques are already well established in the context of artificial neural networks and, indeed, on-going detector characterisation work aims to perform such an analysis.

Multiple detector case

A potential issue with this search is in fact the prevalence of instrumental ring-downs already present in the interferometer data. Unless such features can be vetoed using known instrumental couplings, for example [23],

the only way to distinguish these from the targeted gravitational wave ring-down is to search for coincidences between multiple detectors.

Here, we benefit again from the simplicity of the Bayesian formalism. In the single detector case outlined in this work, we aim to compute the posterior probability for some gravitational wave model, given the interferometer data and some background information. In the multi-detector case we still seek the posterior probability for some model but now using the information contained in each detector’s output. Suppose then that we have some gravitational wave model M_{GW} and detector outputs D_1 and D_2 . We can immediately write down the posterior for M_{GW} using Bayes’ theorem

$$p(M_{\text{GW}}|D_1, D_2, I) = \frac{p(M_{\text{GW}}|I)p(D_1, D_2|M_{\text{GW}}, I)}{p(D_1, D_2|I)}, \quad (27)$$

where the gravitational wave model M_{GW} factors in the appropriate detector response functions for the source sky position and for detectors with uncorrelated output, the joint probabilities are the products of the individual probabilities. For N detectors

$$p(M_{\text{GW}}|\{D\}, I) = p(M_{\text{GW}}|I) \prod_{i=1}^N \frac{p(D_i|M_{\text{GW}}, I)}{p(D_i|I)} \quad (28)$$

and we can again eliminate the denominator by comparing the relative probabilities of different models via the odds ratio. Notice, however, that if the probability from one detector is very large but low in the other detectors it is still possible to get a high posterior across all the detectors. It would, therefore, be sensible to apply a cut to the data such that the odds must cross some threshold for each individual detector before considering the multi-detector case.

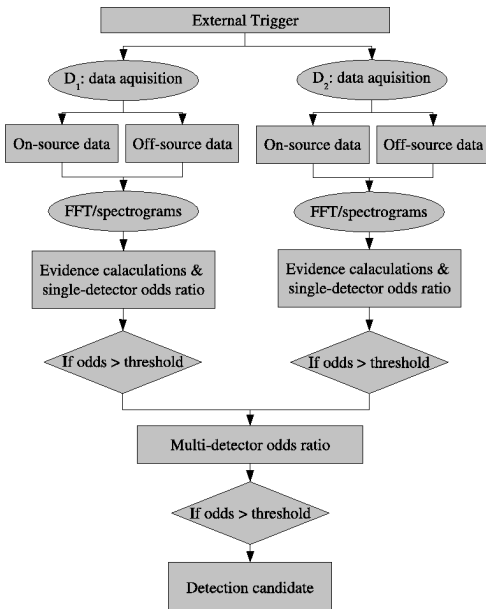


FIG. 13: Planned multi-detector, evidence-based analysis pipeline.

Analysis pipeline

Finally, we present the outline for a planned analysis pipeline in Fig. 13. Here, we assume a network of two detectors and that there is no correlation in the output from each.

Upon reception of an external trigger, such as a pulsar glitch or soft γ -ray repeater flare, we would retrieve interferometer data from near the event (on-source data). The length of data required will typically depend on the time resolution of the external trigger. Additionally, we require data preceding the external trigger to provide some estimate of the background odds ratio and hence set the threshold for the desired false alarm probability.

Following the acquisition of both on and off-source data for each detector, we transform to the Fourier domain and construct spectrograms of each. From here, the methods outlined in this work can be used to compute the evidences for each gravitational wave and glitch model and the odds ratio can be computed for each detector using on and off-source data.

If the odds in *both* detectors cross some appropriate threshold, then we can go on to calculate the multi-detector odds ratio. If this multi-detector odds ratio also crosses a threshold set from off-source data then we have a candidate detection.

Alternatively, if the odds ratio from just one of the detectors in the network crosses the respective threshold, then there is probably good evidence for a glitch. Further examination of the odds ratios for each glitch model may reveal its nature and the information could conceivably

be used to update the prior on that particular model in future studies.

VI. CONCLUDING REMARKS

We have examined the feasibility of using a Bayesian evidence discriminator in an externally-triggered search for gravitational waves produced by neutron star quasi-normal mode ring-downs. The evidence may be thought of as the total probability of the data given some model. By comparing the evidences for competing models via the ‘odds ratio’, we can naturally make maximal use of prior information regarding the source as well as any information available from detector characterisation studies.

This is particularly important in the single-detector case. Here there may be instrumental transients or ‘glitches’ which would otherwise generate a detection candidate in algorithms which only look for consistency with the target model. We begin with a simple formulation of the odds ratio, O_{12} , where we compare the probability of a noisy ring-down model with the probability of noise alone. We find this yields a 50% detection efficiency for ring-downs with frequency 2 kHz, decay time 0.2 s and signal-to-noise ratio $\rho = 5.5$ for a 1% false alarm probability in Gaussian white noise of amplitude spectral density $10^{-22} \text{ Hz}^{-1/2}$. This is within an agreement of 1σ with the signal-to-noise ratio threshold of 5.75 required for the same false alarm probability using matched filtering, described in section IV C.

Assuming $10^{-11} M_{\odot} c^2$ is emitted as gravitational waves, these sources are observable to a distance of 8.9 pc. Conversely, a source at a distance of 15 kpc requires an energy of $2.8 \times 10^{-5} M_{\odot} c^2$ to be emitted as gravitational waves. This is several orders of magnitude greater than the typical energy we might expect from a pulsar glitch, making these sources a more attractive target for next-generation detectors such as advanced LIGO [24] and GEO-HF [25]. If, for example, we consider advanced LIGO with a factor ~ 10 improvement in sensitivity over LIGO, the energy required to produce the same signal-to-noise ratio drops to $\sim 5 \times 10^{-8} M_{\odot} c^2$. While this is still well below our fiducial pulsar glitch gravitational wave energy of $10^{-11} M_{\odot} c^2$, it is comparable to the gravitational wave energy expected to be emitted following the axisymmetric collapse of the core of a massive star, some fraction of which will be channelled into the oscillatory modes of the proto-neutron star [26, 27]. Again, if we assume the fiducial gravitational wave energy of $10^{-11} M_{\odot} c^2$, advanced LIGO will be sensitive to neutron star ring-downs at a distance of 202 pc.

We find the simple comparison between white noise and ring-downs is insufficient to discriminate between different types of signal and will be fooled by any transient departure from Gaussianity in the noise. Robustness is improved by including a toy catalogue of glitch models (a sine-Gaussian). The odds ratio may then be extended (i.e., O_{123}) to mitigate the effects of these un-

wanted signals at a relatively small sensitivity cost: a ring-down signal-to-noise ratio of $\rho = 7.0$ is now required for the 50% ring-down detection efficiency and 1% false alarm probability due to Gaussian white noise, so that the total gravitational wave energy required for 50% detection probability of a source at 15 kpc is now $4.6 \times 10^{-5} M_{\odot} c^2$ and the observable range is now 6.9 pc. With advanced LIGO sensitivity, these estimates improve to $9.8 \times 10^{-8} M_{\odot} c^2$ and 151 pc for the energy in gravitational waves and the observable range, respectively.

We find that beyond a sine-Gaussian signal-to-noise ratio of $\rho \approx 6$ the value of the odds ratio O_{123} remains approximately constant and we can set a single, maximum false alarm probability due to sine-Gaussians of 45%. As we have discussed, this may seem rather high but it does not seem unreasonable given that it assumes the presence of a sine-Gaussian signal in the first place. It is also important to emphasise that the probability of detecting a ring-down only increases (provided the amplitude is well within the range allowed by the prior), whereas the false alarm probability for both sine-Gaussians and white noise remains constant. Table III compares sensitivity estimates and false alarm probabilities for both cases.

Finally, we have made mention of some of the future work required to use the methodology in this work in a search for gravitational waves. For the single detector case, it will be necessary to acquire an appropriate catalogue of glitch models and associated prior probabilities for their parameters. The extension to the multi-detector

case will require considerable modification to the waveform model to account for light travel time between detectors and the appropriate antenna response functions for a given sky location. For this search, we are at an advantage in that we know the source location and event time, and hence the factors introduced by the antenna response and time delay are known. We note, however, that if this was not so, as would be the case for an all-sky search or where we had a trigger but no source location, it would be necessary to marginalise over the source location which would significantly complicate the evidence calculation.

With a clear idea of the future analysis pipeline, the next step is to characterise the algorithm response using real interferometer data and all the consequences of non-Gaussian noise.

Acknowledgments

The authors are very grateful to the LIGO scientific collaboration for their support. We are indebted to many of our colleagues for their fruitful discussion and advice. In particular, we would like to thank Patrick Sutton and Szabolcs Marka for their valuable comments on the manuscript and John Veitch for his insight and lively discussion regarding the subject matter. This work has been supported by the UK Particle Physics and Astronomy Research Council.

-
- [1] K. S. Thorne, *Astrophys. J.* **158**, 1 (1969).
- [2] K. D. Kokkotas, T. A. Apostolatos, and N. Andersson, *Mon. Not. R. Astron. Soc.* **320**, 307 (2001), gr-qc/9901072.
- [3] J. A. de Freitas Pacheco, *Astron. Astrophys.* **336**, 397 (1998), astro-ph/9805321.
- [4] N. Andersson and K. D. Kokkotas, *Mon. Not. R. Astron. Soc.* **299**, 1059 (1998), gr-qc/9711088.
- [5] N. Andersson, *Classical and Quantum Gravity* **20**, 105 (2003), .
- [6] H. Lück, M. Hewitson, P. Ajith, B. Allen, P. Aufmuth, C. Aulbert, S. Babak, R. Balasubramanian, B. W. Barr, S. Berukoff, et al., *Classical and Quantum Gravity* **23**, 71 (2006).
- [7] D. Sigg and (for the LIGO Science Collaboration), *Classical and Quantum Gravity* **23**, S51 (2006), URL <http://stacks.iop.org/0264-9381/23/S51>.
- [8] E. Tournefier and VIRGO Collaboration, in *SF2A-2005: Semaine de l'Astrophysique Francaise*, edited by F. Casoli, T. Contini, J. M. Hameury, and L. Pagani (2005), pp. 539–+.
- [9] L. Samuelsson and N. Andersson, *Mon. Not. R. Astron. Soc.* (2006), astro-ph/0609265.
- [10] O. Benhar, V. Ferrari, and L. Gualtieri, *Phys. Rev. D* **70**, 124015 (2004), astro-ph/0407529.
- [11] J. Middleton, F. E. Marshall, Q. D. Wang, E. V. Gotthelf, and W. Zhang, *Astrophys. J.* **652**, 1531 (2006), astro-ph/0605007.
- [12] *Jodrell Bank Crab Pulsar Monthly Ephemeris* <http://www.jb.man.ac.uk/~pulsar/crab.html>.
- [13] R. Dodson, D. Lewis, and P. McCulloch, *ArXiv Astrophysics e-prints* (2006), astro-ph/0612371.
- [14] Y. E. Nakagawa, A. Yoshida, K. Hurley, J.-L. Atteia, M. Maetou, T. Tamagawa, M. Suzuki, T. Yamazaki, K. Tanaka, N. Kawai, et al., *ArXiv Astrophysics e-prints* (2007), astro-ph/0701701.
- [15] K. S. Cheng, D. Pines, M. A. Alpar, and J. Shaham, *Astrophys. J.* **330**, 835 (1988).
- [16] L. M. Franco, B. Link, and R. I. Epstein, *Astrophys. J.* **543**, 987 (2000), astro-ph/9911105.
- [17] K. A. van Riper, R. I. Epstein, and G. S. Miller, *Astrophys. J. Lett.* **381**, L47 (1991).
- [18] R. Dodson, D. R. Lewis, and P. M. McCulloch, in *ASP Conf. Ser. 271: Neutron Stars in Supernova Remnants* (2002), pp. 357–+.
- [19] A. G. Lyne, R. S. Pritchard, and F. Graham-Smith, *Mon. Not. R. Astron. Soc.* **265**, 1003 (1993).
- [20] K. Hurley, S. E. Boggs, D. M. Smith, R. C. Duncan, R. Lin, A. Zoglauer, S. Krucker, G. Hurford, H. Hudson, C. Wigger, et al., *Nature* **434**, 1098 (2005), astro-ph/0502329.
- [21] *LIGO Algorithm Library*, <http://www.lsc-group.phys.uwm.edu/daswg/projects/lal.html>, <http://www.lsc-group.phys.uwm.edu/daswg/projects/lalapp>

- [22] L. M. Goggin and the LIGO Scientific Collaboration, *Classical and Quantum Gravity* **23**, 709 (2006).
- [23] P. Ajith, M. Hewitson, J. R. Smith, and K. A. Strain, *Classical and Quantum Gravity* **23**, 5825 (2006), gr-qc/0605079.
- [24] P. Fritschel, in *Gravitational-Wave Detection. Edited by Cruise, Mike; Saulson, Peter. Proceedings of the SPIE, Volume 4856, pp. 282-291 (2003).*, edited by M. Cruise and P. Saulson (2003), pp. 282–291.
- [25] B. Willke, P. Ajith, B. Allen, P. Aufmuth, C. Aulbert, S. Babak, R. Balasubramanian, B. W. Barr, S. Berukoff, A. Bunkowski, et al., *Classical and Quantum Gravity* **23**, 207 (2006).
- [26] V. Ferrari, G. Miniutti, and J. A. Pons, *Mon. Not. R. Astron. Soc.* **342**, 629 (2003), astro-ph/0210581.
- [27] H. Dimmelmeier, J. A. Font, and E. Müller, *aap* **393**, 523 (2002), astro-ph/0204289.